Check for updates

From 20% single-junction organic photovoltaics to 26% perovskite/organic tandem solar cells: self-assembled hole transport molecules matter†

Xiaokang Sun,‡[ab] Fei Wang,‡[a] Guo Yang,‡[a] Xiaoman Ding,[a] Jie Lv,[a] Yonggui Sun,[a] Taomiao Wang,[a] Chuanlin Gao,[c] Guangye Zhang,[c] Wenzhu Liu,[d] Xiang Xu,[a] Soumitra Satapathi, [e] Xiaoping Ouyang,[b] Annie Ng, [f] Long Ye, [g] Mingjian Yuan, [h] Hongyu Zhang [i] and Hanlin Hu [*a]

Achieving high efficiency in single-junction organic solar cells (OSCs) and tandem solar cells (TSCs) significantly relies on hole transport layers constructed from self-assembled molecules (SAMs) with a well-ordered, face-on alignment. In this study, we enhanced the ordered stacking of a SAM layer by leveraging the interaction between the π-conjugated backbone of SAMs and volatile solid additives with opposing electrostatic potentials. This approach induced a highly ordered stacking of the SAM layer, as confirmed by the presence of multiple X-ray scattering peaks and an increased Herman orientation factor from 0.402 to 0.726 after the evaporation of solid additives. This optimization not only strengthened hole transport properties but also positively influenced the film formation kinetics of the upper active layer, improving morphology and vertical phase separation. As a result, we achieved a notable power conversion efficiency (PCE) of 20.06% (certified 19.24%) in PM6:BTP-eC9 binary OSCs, with a further breakthrough PCE of 26.09% in perovskite-organic tandem solar cells (TSCs).

Broader context

Achieving high efficiency in both single-junction organic solar cells (OSCs) and tandem solar cells (TSCs) significantly relies on hole transport layers (HTLs) constructed from self-assembled molecules (SAMs) with a well-ordered, face-on alignment. Herein, we successfully demonstrated a facile strategy to regulate the stacking of SAM layers *via* incorporating a volatile solid additive. The opposing electrostatic potentials of (4PADCB) SAMs and (1,3,5-trichlorobenzene) TCB intensified their interaction, leading to a highly ordered staking of SAMs with improved face-on orientation after the evaporation of the solid additive, which enhanced hole transport capacity and influenced the film formation kinetics of the upper active layer. As a result, the binary OSC device with TCB-treated SAMs exhibited a superior PCE of 20.06% with an impressive FF of 80.64%. Moreover, we achieved a remarkable PCE of 26.09% in a perovskite-organic tandem solar cell utilizing the TCB-treated SAMs. This study provides a facile approach to regulate the stacking and ordering of the SAM layer with solid additives to improve the performance of photovoltaic devices in single-junction and tandem cells.

Introduction

Organic solar cells (OSCs) are rapidly advancing next-generation photovoltaic technology, offering advantages such as semitransparency, flexibility and cost-effectiveness.[1,2] With the development of light-absorbing materials and advances in device engineering, the power conversion efficiency (PCE) of state-of-the-art OSCs has surpassed the 20% milestone.[3–7]

[a] *Hoffmann Institute of Advanced Materials, Shenzhen Polytechnic University, 7098 Liuxian Boulevard, Shenzhen, 518055, China. E-mail: hanlinhu@szpu.edu.cn*

[b] *School of Materials Science and Engineering, Xiangtan University, Xiangtan, 411105, China*

[c] *College of New Materials and New Energies, Shenzhen Technology University, Shenzhen, 518118, China*

[d] *Research Center for New Energy Technology, Shanghai Institute of Microsystem and Information Technology, Chinese Academy of Sciences, Shanghai, China*

[e] *Indian Institute of Technology Roorkee, Uttarakhand, 247667, India*

[f] *Department of Electrical and Computer Engineering, School of Engineering and Digital Sciences, Nazarbayev University, Astana 010000, Kazakhstan*

[g] *School of Materials Science & Engineering, Tianjin Key Laboratory of Molecular Optoelectronic Sciences, Collaborative Innovation Center of Chemical Science and Engineering (Tianjin), Tianjin University, Tianjin, 300350, China*

[h] *College of Chemistry, Nankai University, Tianjin, China*

[i] *State Key Laboratory of Supramolecular Structure and Materials, College of Chemistry, Jilin University, Changchun, 130012, China*

† Electronic supplementary information (ESI) available. See DOI: https://doi.org/10.1039/d4ee05533k

‡ X. Sun, F. Wang and G. Yang contributed equally to this work.

2536 | *Energy Environ. Sci.*, 2025, **18**, 2536–2545

This journal is © The Royal Society of Chemistry 2025

Recent high-performance devices are increasingly built on self-assembled molecules (SAMs) as hole transport layers owing to their excellent hole selectivity and high transmittance in the visible-near-infrared (vis-NIR) region.[8,9] SAM materials primarily consist of anchoring, spacer and functional groups. Anchoring is used to adhere to metal oxides (*e.g.*, indium tin oxide and nickel oxide), while the spacer serves as the structural backbone for connecting the anchoring and functional groups. Functional groups are essential for adjusting surface characteristics, including hole transport capability, energy level and surface energy.[10,11]

Additionally, for a simple one-step spin coating process to prepare the SAM layer, an overlayer is formed with a thickness of several nanometers, which adheres on metal oxides *via* both covalent bonds and van der Waals force.[6,12] This indicates that there is a coverage of the substrate through anchoring and stacking of upper-layer molecules. The ordered stacking in SAM layers directly determines the performance of the photovoltaic device.[11] Recent studies have demonstrated that the ordered aggregation and orientation of the SAM layer could further improve hole-extraction capability. For example, Jen *et al.* replaced the alkyl linker of (4-(7*H*-dibenzo[*c,g*]carbazol-7-yl)phenyl)-phosphonic acid (CbzNaphPPA) with a phenyl group to improve molecular rigidity. This modification significantly improved the intermolecular interaction within SAMs, leading to the formation of *H*-aggregates and a notable enhancement in hole mobility.[12] Liu *et al.* designed a non-fused ring SAM that achieved a face-on orientation of the π-functionalized backbone (aligned parallel to ITO) through its double-phosphate anchoring groups.[13] This favorable orientation enhances charge transfer and promotes hole collection.[14–16] However, there is limited research on methods to efficiently regulate the ordered stacking of SAM layers, and accurately characterizing the internal feature of SAM layers remains a challenge.

In recent years, the volatile solid additive strategy has successfully regulated the π–π stacking and orientation of active layer molecules in OSCs.[17–21] This strategy leverages the interaction of the additive with the donor or acceptor in the active layer (usually weak interactions) to optimize molecular stacking, and the additive will volatilize during the thermal annealing process. Based on these, it is worth considering that the π-functionalized backbone on SAM may also interact with these additives to effectively regulate π–π stacking. As a proof-of-concept, we selected the (4-(7*H*-dibenzo[*c,g*]carbazol-7-yl)butyl)phosphonic acid (4PADCB) as the SAM and 1,3,5-trichlorobenzene (TCB) as the additive.[14,22] The π-functionalized backbone of SAM exhibited strong electronegativity, while the benzene ring of TCB showed a relatively positive potential distribution, facilitating the interaction between the SAM and the additive. After the thermal annealing process, an ordered stacking with the face-on orientation formed in the SAM layer, which enhanced the hole transport capacity and the stability under long-time operation. This modification also regulated the film formation kinetics of the active layer, resulting in improved crystallinity and ideal vertical phase separation in the blend film. Consequently, the device with TCB-treated SAMs achieved a superior PCE of 20.06% with a high fill factor (FF) of 80.64%.

In perovskite-organic tandem solar cells (TSCs), the application of additive strategy resulted in a significant PCE of 26.09%.

Results and discussion

Molecular properties and interactions

The chemical structures of 4PADCB and TCB are shown in Fig. 1a. While 4PADCB demonstrated successful application in perovskite solar cells (PSCs),[14] TCB served as a volatile additive that optimizes the active layer morphology in OSCs.[22] TCB, with a decomposition temperature (T_d, 5% weight loss) of 42 °C, fully evaporates at 100 °C (Fig. S1, ESI†), indicating its complete removal during the thermal annealing (TA) process of the SAM layer at 130 °C. To verify this, we performed Fourier transform infrared (FTIR) spectroscopy to trace any residual TCB after the TA process. As shown in Fig. 1b, the characteristic FTIR peaks of TCB at 656, 1096, 1560 and 3081 cm^{-1} persisted in the TCB-treated SAM without TA, but they vanished post annealing, confirming the *in situ* removal of TCB during the TA process.

To further investigate the interaction between SAM and TCB, we performed density functional theory (DFT) calculations of the electrostatic potential (ESP) distributions using the B3LYP/6-31G(d,p) basis set.[23,24] Fig. 1a illustrates that the DCB core exhibits strong electronegativity, while the benzene ring in TCB displays a relatively positive potential due to chlorine atom contributions.[15,22] The average ESP values ($\bar{V}$) for the DCB core and TCB were −1.11 kcal mol^{-1} and 2.33 kcal mol^{-1} (Fig. S2 and Table S1, ESI†), suggesting that there were significant intermolecular interactions.[25] In the assembled structure (Fig. 1c), TCB aligned preferentially with the DCB core, forming a closely packed conjugated conformation, as evidenced by a stacking distance of 3.31 Å and a prominent green plane in the non-covalent interactions analysis.[26] Additionally, reduced density gradient (RDG) and $\text{Sin}(\lambda_2)\rho$ analyses (Fig. S3, ESI†) highlighted the attractive interactions between SAM and TCB.[27,28] The FTIR spectra (Fig. S4, ESI†) further corroborated this interaction, where the vibration peaks near 1460–1470 cm^{-1} and 1520–1530 cm^{-1} corresponded to the stretching vibrations of the carbazole ring, respectively.[29] The carbazole ring vibrations shifted slightly from 1526 and 1467 cm^{-1} to 1527 and 1469 cm^{-1} after TCB treatment, indicating preferential interaction between TCB and the DCB core. This interaction was further confirmed by the ^{1}H NMR data (Fig. S5, ESI†), where the peak at 7.5–7.7 ppm represented the carbazole ring of SAM. A noticeable shift of the SAM peaks could be observed after TCB treatment. Collectively, the DFT and experimental findings suggested that TCB promoted compact molecular packing within the SAM by interacting with the DCB core.[12,17,27]

Grazing-incident wide-angle X-ray scattering (GIWAXS) technique was employed to investigate the molecular packing and orientation of SAMs with TCB treatment (Fig. 1d). Both control and TCB-treated SAM exhibited face-on orientation features with the conjugation backbone parallel to the substrate. Scattering profiles along the out-of-plane (OOP) directions were obtained from GIWAXS patterns (Fig. S6, ESI†) using SGTools

This journal is © The Royal Society of Chemistry 2025

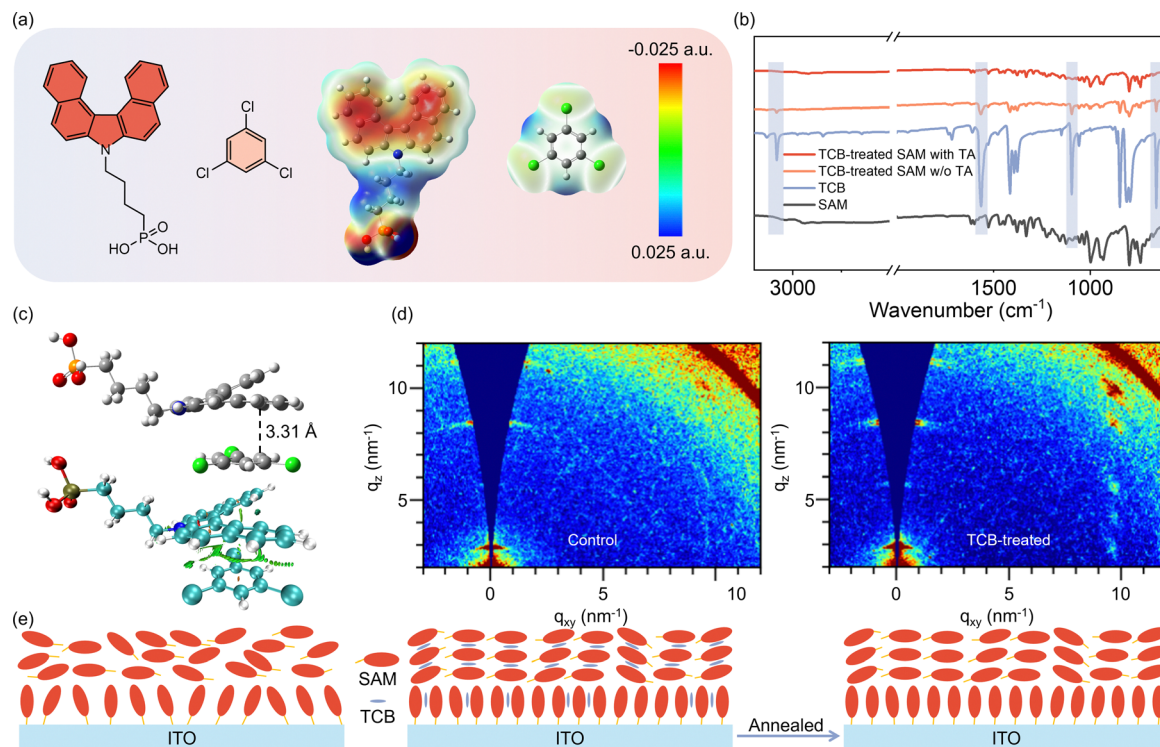*Energy Environ. Sci.*, 2025, **18**, 2536–2545 | **2537**

Fig. 1 (a) Chemical structures and ESP distributions of 4PADCB and TCB. (b) FTIR spectra to trace the additive TCB residue in the SAM layer. (c) Visualization analysis of non-covalent interactions. (d) GIWAXS patterns of the control and TCB-treated SAM layer. (e) Schematic plot showing that a more ordered stacking with a face-on feature formed after TCB-treatment.

software,[30] revealing the emergence of multiple scattering peaks in the TCB-treated SAM, indicating the formation of highly parallel-oriented period structures. Additionally, Bragg rods appeared at $q_{xy} \approx 9.5$ nm^{-1} in patterns of TCB-treated SAM (Fig. S6, ESI†) form an angle of approximately 45° with respect to the in-plane direction, providing further insights into the ordered structure induced by TCB treatment. Consistent with previously reported studies,[31,32] this suggests the presence of both 2D hexagonal phase and cubic phase (Fig. S7, ESI†). In the hexagonal phase, the lattice parameter, deduced from the location of the (01) peak, indicates a lattice constant of 0.65 nm. For the cubic phase, the lattice parameter calculated along (10) is 2.14 nm. Compared to the control SAM layer, the enhanced ordered stacking of the SAM layer after TCB-treatment can improve charge transfer, reduce charge carrier recombination, and facilitate effective hole collection.[12,13,15,16] The Herman orientation factor (f) was used to quantify the SAM orientation,[33] with the TCB-treated SAM exhibiting a significantly higher f value of 0.726 than that of the control SAM's 0.402 (Fig. S6, ESI†). Subsequently, we evaluated the thermal stability of SAM layers, as shown in Fig. S8 (ESI†). The main diffraction peak of the fresh SAM film is located at 4.0°, which is consistent with the GIWAXS patterns. After heating at 55 °C for 20 hours, the diffraction peak of the control SAM layer noticeably weakened, indicating a decrease in the ordered conformation of the film. In contrast, the diffraction peak of the TCB-treated SAM layer remained almost unchanged after heating, implying a strong and stable stacking mode. As depicted in Fig. 1e, the volatile solid additive strategy optimized intermolecular

interactions and molecular aggregations behavior in the SAM layer, resulting in a highly ordered face-on orientation. This improved packing enhances hole mobility, reduces charge carrier recombination at the SAM/active layer interface, and ultimately improves the device performance.

Optoelectronic properties and photovoltaic performance of the OSCs

Peak force tunneling atomic force microscopy (PF-TUNA) was performed to observe the surface electronic properties of both control and TCB-treated SAM. In Fig. 2a–c, TCB-treated SAM showed an average surface current of about 2.0 nA higher than that of control SAM (about 1.2 nA). Also, from the J–V dark curves of the device with the structure of ITO/control and TCB-treated SAM/Ag (Fig. S9, ESI†), TCB-treated SAM displayed a higher slope value of 5.71 than that of 4.98 based on control SAM, indicating reduced contact resistance and charge transport.[34–37] Binary OSCs with the ITO/SAM/PM6:BTP-eC9/C60/BCP/Ag architectures were fabricated to assess the impact of TCB on the photovoltaic performance. Fig. 2d and Table 1 present the J–V curves and photovoltaic parameters for the best-performing devices (more detailed data were available in Tables S2 and S3, ESI†). The statistical distribution of PCE over ten devices is shown in Fig. 2e. The control device achieved a champion PCE of 19.35%, with a J_{SC} of 28.43 mA cm^{-2}, a V_{OC} of 0.859 V, and an FF of 79.25%. In contrast, the device based on the TCB-treated SAM reached a superior PCE of 20.06% with a V_{OC} of 0.863 V, a J_{SC} of 28.83 mA cm^{-2} and an FF of 80.64%. A certified efficiency of

19.24% (Fig. S10, ESI†) was achieved by the South China National Center of Metrology-Guang Dong Institute of Metrology. These values including PCE and FF represented some of the highest reported for binary OSCs. According to the EQE spectra (Fig. 2f), the OSC device based on TCB-treated SAM exhibited an integrated current density of 28.03 mA cm^{-2}, while the control SAM-based device reached 27.58 mA cm^{-2}. Both values closely aligned with the J_{SC} values obtained from J–V curves, showing a mismatch of less than 5%. Fig. 2g illustrates the performance of unpackaged devices based on control and TCB-treated SAMs under continuous illumination at 100 mW cm^{-2}. The TCB-treated SAM device demonstrated improved stability, which can be attributed to the more ordered stacking of SAMs.[12,13,35] Notably, a significant degradation occurred during the initial stage of the stability test, which may be due to the photochemical reaction at the interface and the change in the work function of ITO under illumination.[6,38] To further evaluate the versatility of TCB treatment strategy, various active layer systems were tested, comparing the

performance of devices based on the control and TCB-treated SAM. The violin plot (Fig. 2h) and corresponding parameters (Table S4, ESI†) clearly demonstrated that the TCB-treated SAM devices outperformed the control devices.

The Mott–Schottky characteristics were analyzed by plotting the C^{-2}–V relationship (Fig. 3a) to determine the built-in voltage (V_{bi}) for devices based on the control and TCB-treated SAM. The V_{bi} values measured 0.719 V for control device and 0.743 V for the device based on the TCB-treated SAM, implying reduced Schottky barrier at the ITO/active layer interface, leading to a higher V_{OC} value.[8,35] The Nyquist plots were measured for devices based on the control and TCB-treated SAM in the dark (Fig. S11, ESI†). The recombination resistance (R_{rec}) of the device with TCB-treated SAM was significantly higher than that of the control device, indicating effectively suppressed carrier recombination.[39] As shown in Fig. 3b, the hole mobility μ_h of the device based on TCB-treated SAM was 7.24×10^{-4} cm^2 V^{-1} s^{-1}, exceeding the control device's 5.97×10^{-4} cm^2 V^{-1} s^{-1}, confirming that TCB treatment enhanced the hole transport of SAMs. The dark J–V
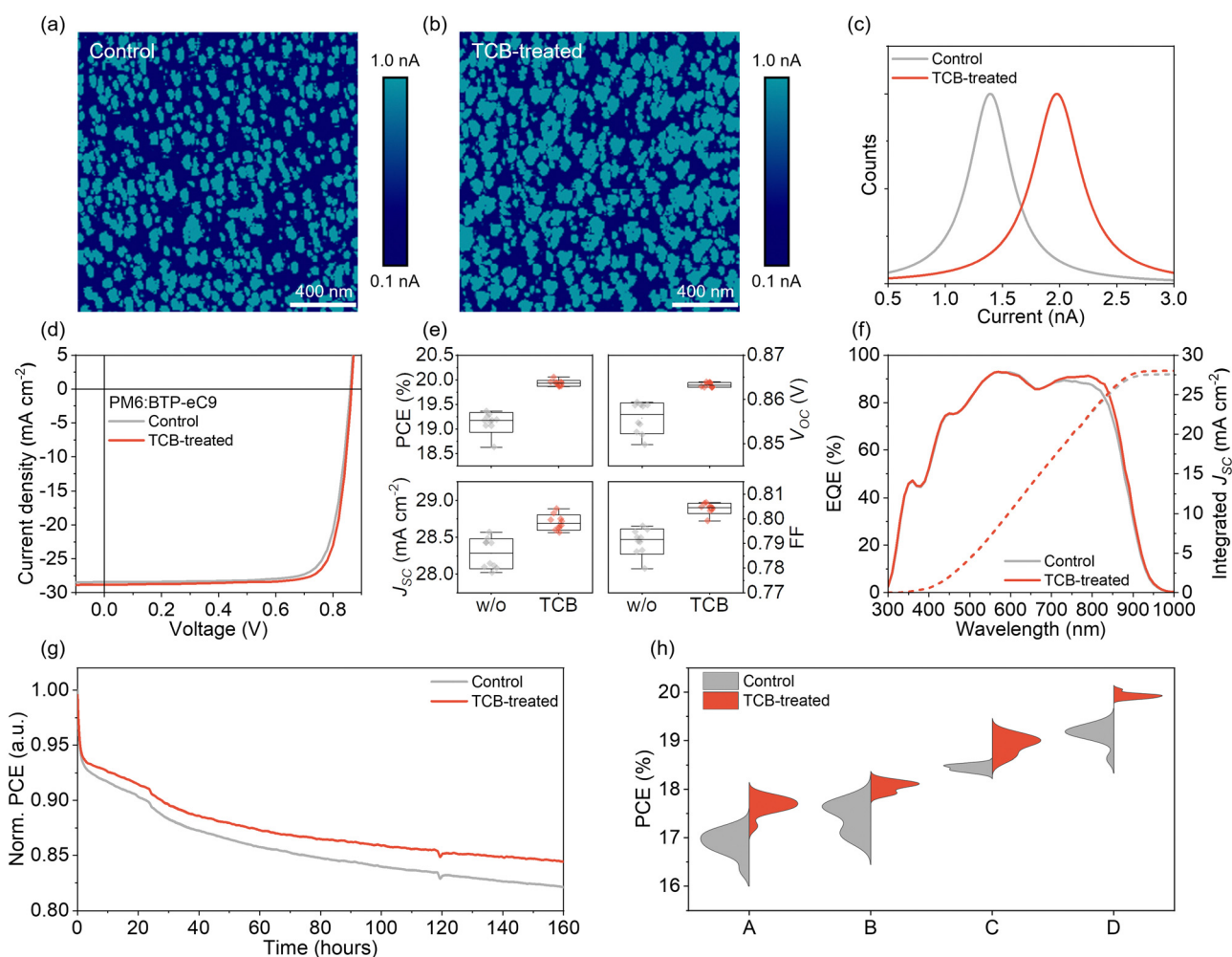

Fig. 2 PF-TUNA current images of (a) the control and (b) TCB-treated SAM. (c) Corresponding surface current signals. (d) J–V curves. (e) Statistics of PCE for devices based on the control and TCB-treated SAM layer. (f) EQE spectra. (g) Photostability of devices based on the control and TCB-treated SAM layer. (h) Violin plots of PCE distribution of devices based on the control and TCB-treated SAM layer (A: PM6:Y6; B: PM6:Y6:PC$_{71}$BM; C: PM6:L8-BO; D: PM6:BTP-eC9).

Table 1 Photovoltaic performance of PM6:BTP-eC9 OSCs based on the control and TCB-treated SAMs

	V_{OC} (V)	J_{SC} (mA cm^{-2})	J_{SC}^{Cal} (mA cm^{-2})	FF	PCE (average) (%)
Control	0.859 (0.856 ± 0.003)	28.43 (28.28 ± 0.20)	27.58	79.25 (79.08 ± 0.51)	19.35 (19.14 ± 0.20)
TCB-treated	0.863 (0.863 ± 0.001)	28.83 (28.70 ± 0.10)	28.03	80.64 (80.43 ± 0.21)	20.06 (19.93 ± 0.06)

curves (Fig. 3c) indicated that the TCB-treated SAM device exhibited a lower leakage current under reverse bias, suggesting improved diode characteristics and a notable reduced leakage.[40] Transient photocurrent (TPC) and transient photovoltage (TPV) measurements (Fig. 3d and e) revealed that the charge extraction time for the TCB-treated SAM device was 0.197 μs, compared to 0.296 μs for the control, while its carrier lifetime was longer at 5.43 μs *versus* 3.50 μs for the control. This suggested that TCB treatment suppressed charge recombination and

enhanced charge extraction in the corresponding devices. The exciton dissociation and charge collection behaviors were evaluated by analyzing the relationship between photocurrent density (J_{ph}) and photovoltage (J_{eff}) (Fig. 3f). The device with TCB-treated SAMs demonstrated a higher exciton dissociation efficiency (P_{diss} = 98.51%) than that of the control device (P_{diss} = 96.90%). Additionally, the exciton collection probability (P_{coll}) values for the control and TCB-treated SAM devices were 89.96% and 95.18%, respectively. The higher values of P_{diss} and P_{coll} indicated more
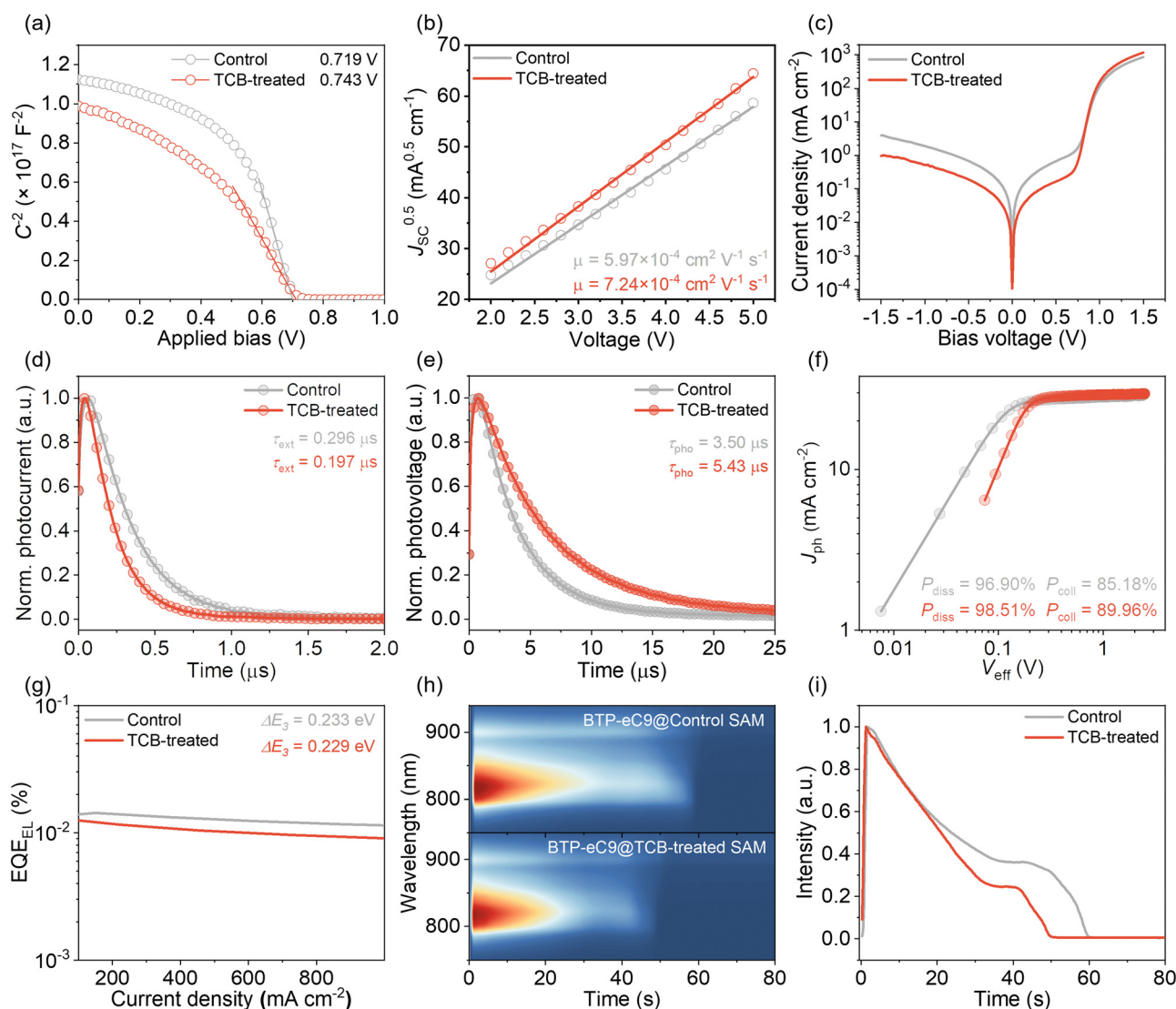

Fig. 3 (a) Mott−Schottky curves of devices based on the control and TCB-treated SAM layer. (b) SCLC of hole-only devices based on the control and TCB-treated SAM layer. (c) Dark *J−V* curves. (d) and (e) TPC and TPV of devices based on the control and TCB-treated SAM layer. (f) J_{ph} (photocurrent density) plotted against V_{eff} (effective voltage) for devices based on the control and TCB-treated SAM layer. (g) EQE$_{EL}$ plots of devices based on the control and TCB-treated SAM layer. (h) *In situ* PL of neat BTP-eC9 films on control and TCB-treated SAM and (i) the time evolution of PL intensity.

2540 | *Energy Environ. Sci.*, 2025, **18**, 2536–2545

This journal is © The Royal Society of Chemistry 2025

efficient exciton dissociation and carrier collection in blend films on the TCB-treated SAM, which contributed to the increased J_{SC} value. Light-intensity dependence of V_{OC} and J_{SC} was also examined (Fig. S12, ESI†), with the TCB-treated SAM device showing a superior slope of 1.06 kT q^{-1} to 1.10 kT q^{-1} for the control. Additionally, the TCB-treated SAM device had a higher α value of 0.990, compared to 0.989 for the control, suggesting reduced trap-assisted and bimolecular recombination in the TCB-treated SAM device. Energy loss was assessed using EQE_{EL} measurements, with non-radiative recombination (ΔE_3) calculated as $-kT/\ln(EQE_{EL})$ (Fig. 3g). The TCB-treated SAM device showed a lower ΔE_3 of 0.229 eV compared to 0.233 eV for the control device. To further clarify the energy disordered within the device, Fourier transform photocurrent spectroscopy-external quantum efficiency (FTPS-EQE) measurements were employed (Fig. S13, ESI†). The TCB-treated SAM device exhibited a lower Urbach energy (E_U) of 23.10 meV compared to 24.21 meV for the control device, indicating reduced energy disorder in the TCB-treated SAM device. The lower nonradiative recombination loss and reduced low energy disorder in the TCB-treated SAM device contributed to enhanced V_{OC}, as shown in the photovoltaic parameters.

Film formation kinetics of active layers

To further investigate the effect of the TCB treatment on the film formation kinetics of the upper active layer, we first conducted the contact-angle measurement to determine the surface energy (γ_S) of both the control and TCB-treated SAM. The results summarized in Fig. S14 and Table S5 (ESI†) indicated that the TCB-treated SAM exhibited a lower γ_S value of 45.12 mN m^{-1} than that of 49.74 mN m^{-1} for the control SAM. These differences in surface energy significantly impacted the film formation process of the upper active layer, resulting in distinct morphologies.[13,41] The *in situ* photoluminescence (PL) was used to study the quenching kinetics of the films on SAM, where changes in PL intensity reflect aggregation-induced emission quenching during the transition from the monomolecular state in solution to the aggregated state in the film.[42] Fig. 3h displays the contour map of the spin-coated neat BTP-eC9 film on both control and TCB-treated SAMs. Notably, the BTP-eC9 exhibits a faster quenching process on TCB-treated SAMs (Fig. 3i), implying a quicker aggregation transition than that of the control SAM. To gain further insights into the aggregation behavior of blend films, *in situ* UV-vis spectroscopy was performed during the spin-coating process. Fig. 4a shows a rapid decrease in absorption as the solution is ejected from the substrate, accompanied by a notable red-shift in the peak position of BTP-eC9. Consistent with *in situ* PL characterization, a faster aggregation process was observed in the blend film on TCB-treated SAMs (Fig. 4d), which promoted the formation of high-crystallinity, pure acceptor phases and enhances charge transport. In contrast, the peak position of PM6 remained relatively stable due to the re-aggregation of the polymer (Fig. S15, ESI†).[43] The thermal annealing process of blend films was monitored *via in situ* UV-vis spectroscopy after

film formation. Contour maps of blend films on the control and TCB-treated SAMs (Fig. 4b and c) show a distinct decrease in absorption intensity and a slight red-shift of the BTP-eC9 peak. This reduction in intensity is attributed to residual solvent evaporation. Fig. 4e and f illustrate the time evolution of peak positions for PM6 and BTP-eC9, revealing opposing trends. PM6 exhibited a blue-shift, while BTP-eC9 showed a red-shift due to increased aggregation of BTP-eC9 and its incorporation into the donor, reducing the packing density of PM6 molecular chains. Notably, BTP-eC9 demonstrated a more pronounced red-shift on the TCB-treated SAM, suggesting that the lower surface energy enhances selective optimization of acceptor domains within the polymer networks. Grazing incidence small-angle X-ray scattering (GISAXS) measurement was conducted to investigate the nanoscale phase separation behavior. The GISAXS patterns are displayed in Fig. S16 (ESI†), and the fitting data are summarized in Table S6 (ESI†). The domain size of the amorphous phase (ξ) in blend films was calculated to be 30.3 nm for the blend film on control SAM and 29.0 nm for the one on TCB-treated SAM. Conversely, the aggregated acceptor domain size (2Rg) increased from 15.6 nm in the control sample to 17.8 nm in the TCB-treated one. These results, combined with the enhanced crystallinity observed, suggested that the TCB-treated SAM improved phase separation in the blend film, potentially aligning more closely with the theoretical exciton diffusion length.[44]

Furthermore, GIWAXS was performed to examine the molecular packing in the blend films on both the control and TCB-treated SAM (Fig. 4g and Fig. S17, ESI†). The fitting parameters derived from the GIWAXS profiles are provided in Table S7 (ESI†). The (010) peak positions for the blend films were located at 17.38 nm^{-1} for the control and 17.45 nm^{-1} for the TCB-treated SAM, corresponding to d-spacings of 0.362 and 0.360 nm, respectively. The crystal coherence lengths (CCL) of the π–π stacking in the blend film were calculated to be 5.47 nm for the control sample and 5.62 nm for the one on TCB-treated SAM, indicating tighter molecular packing and enhanced crystallinity in the film on the TCB-treated SAM. Additionally, surface morphology analysis of the blend film using atomic force microscopy (AFM) (Fig. S18, ESI†) showed that the blend film on TCB-treated SAMs had a smoother surface, with a surface roughness (R_q) of 1.30 nm. Transmission electron microscopic (TEM) images (Fig. S19, ESI†) further revealed an optimized phase separation morphology for the blend film on TCB-treated SAM, consistent with the AFM results. To further understand the vertical phase separation in the blend film, we employed film-depth-dependent light absorption spectroscopy (FLAS). The compositional distributions of PM6 and BTP-eC9 were quantified using the absorption spectrum overlap method (Fig. 4h and i and Fig. S20, ESI†).[45] In the blend film on TCB-treated SAMs, PM6 was more concentrated in the bottom region, while BTP-eC9 was enriched at the top. In contrast to the control, the ratio of PM6 near the TCB-treated SAM interface increased significantly from 58% to 73%. This higher concentration of PM6 at the interface facilitates charge transport and reduces recombination at the electrode surface.[46]
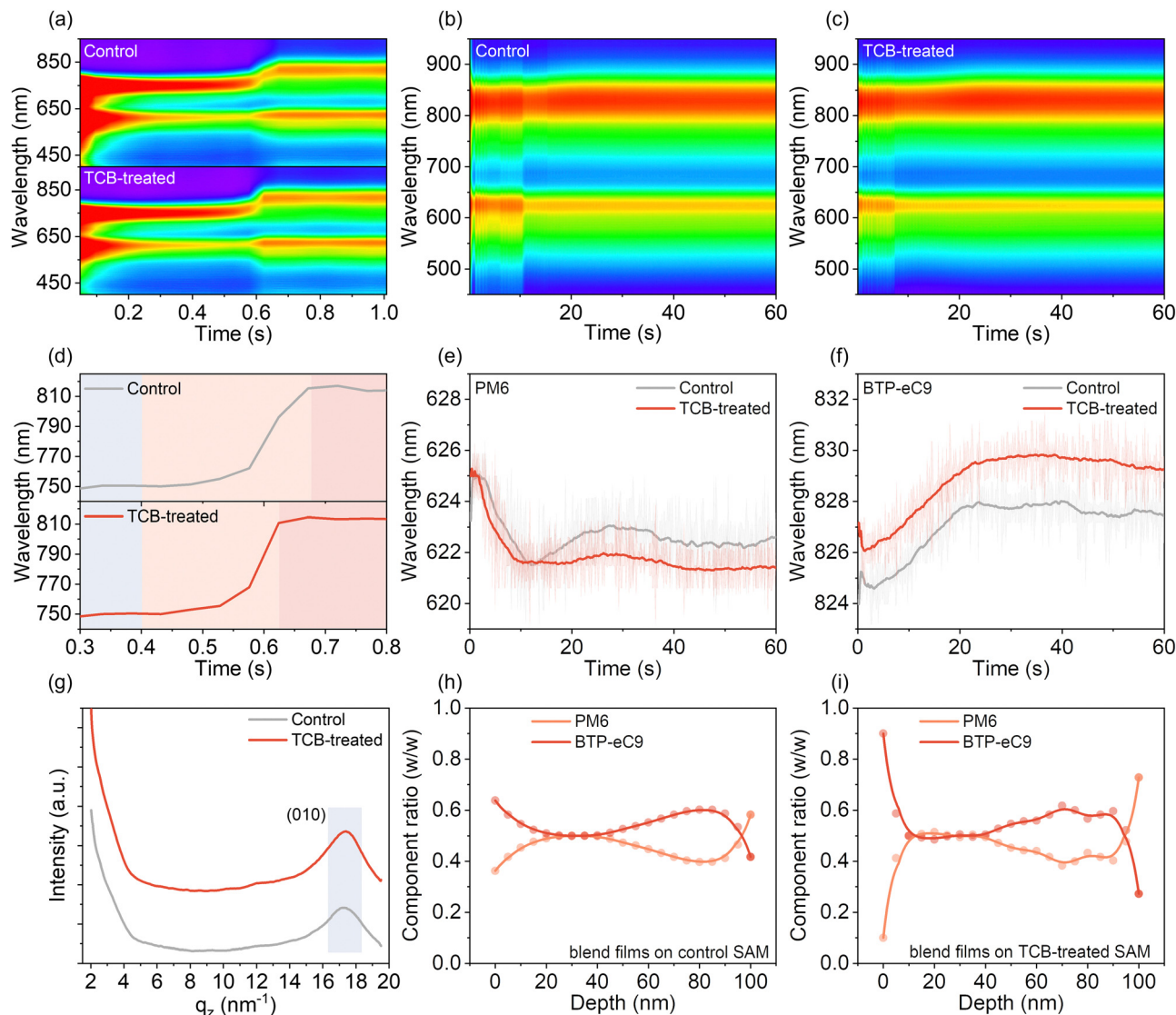
This journal is © The Royal Society of Chemistry 2025

Energy Environ. Sci., 2025, **18**, 2536–2545 | **2541**

Fig. 4 *In situ* absorption of PM6:BTP-eC9 blend films on SAMs (a) during spin-coating and (b) and (c) during thermal annealing process. (d)(f) The time evolutions of the absorption peak of blend films during the spin-coating and thermal annealing processes. (g) GIWAXS scattering profiles of blend films on SAMs along OOP direction. (h) and (i) Calculated component distribution profiles of the blend films based on the control and TCB-treated SAM layer.

Photovoltaic performance of perovskite-organic TSCs

Encouraged by the broad applicability of the TCB treatment strategy across different OPV systems, we extended this approach to fabricate high-performance perovskite-organic TSCs. Fig. 5a illustrates the configuration of the perovskite-organic TSCs, with an ITO/Me-4PACz/wide-bandgap perovskite/C_{60}/BCP/Ag/MoO$_3$/TCB-treated SAM/PM6:BTP-eC9/C_{60}/BCP/Ag structure. Fig. 5b and c and Table S8 (ESI†) present the *J–V* curves, maximum power point (MPP) tracking, and photovoltaic parameters for single-junction OSCs, single-junction PSCs and perovskite-organic TSCs. The champion TSCs achieved an impressive PCE of 26.09%, with a V_{OC} of 2.131 V, a J_{SC} of 14.95 mA cm^{-2}, and a high FF of 81.90%, where both the PCE and FF are among the highest values reported for perovskite-organic TSCs (Fig. S21 and Table S9, ESI†).[47–52] External quantum efficiency (EQE) measurements on the TSCs, as shown in

Fig. 5d, confirmed that the perovskite bandgap is well matched with the OPV layer, adhering to the current matching principle necessary for 2-terminal TSCs. Furthermore, the average PCE of 25.18% was calculated from 30 individual tandem cells fabricated from different batches (Fig. 5e).

Conclusions

In summary, we have successfully demonstrated a facile strategy to regulate the stacking of SAM layers *via* incorporating the volatile solid additive TCB. The opposing electrostatic potentials of SAM and TCB intensified their interaction, leading to a highly ordered stacking of SAMs with improved face-on orientation after the solid additive evaporates, which enhanced the hole transport capacity and influenced the film formation kinetics of the upper active layer. This resulted in an improved crystallinity
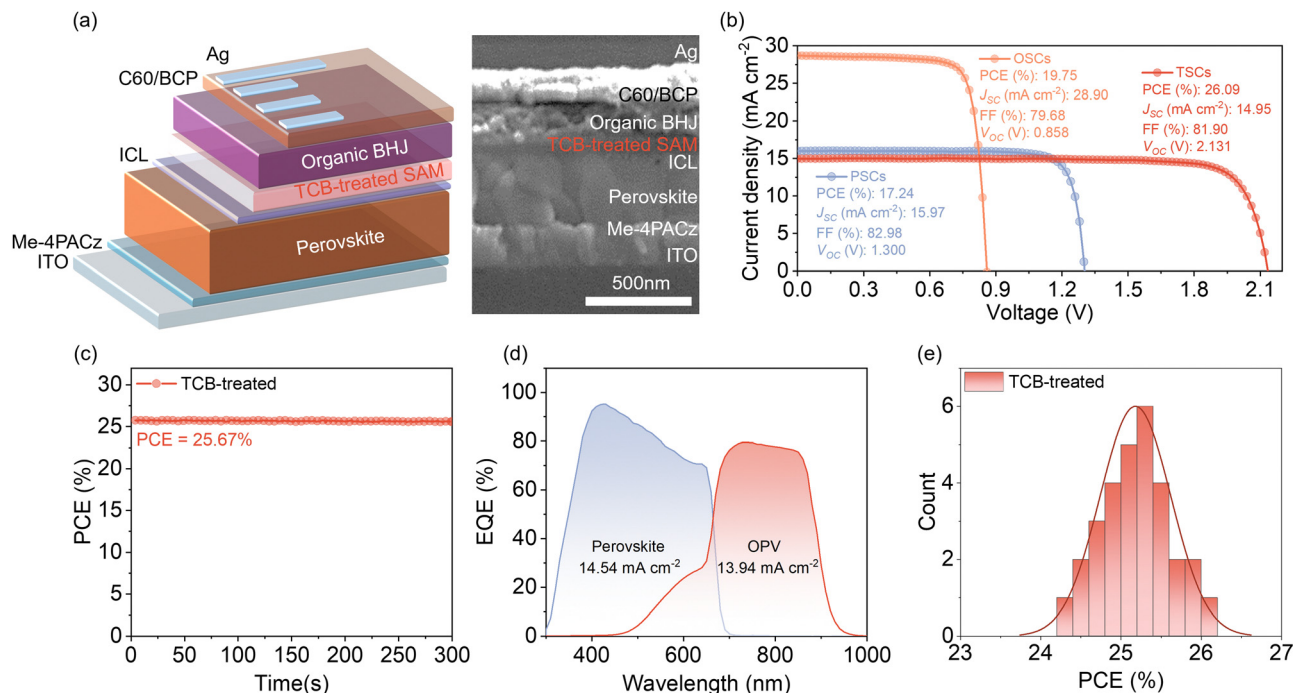
2542 | *Energy Environ. Sci.*, 2025, **18**, 2536–2545

This journal is © The Royal Society of Chemistry 2025

Fig. 5 (a) Schematic and cross-sectional SEM images of the device configuration of the TSC. (b) *J*–*V* curves of champion OSCs, PSCs and TSCs. (c) MPP tracking of TSCs. (d) EQE curves of perovskite and organic subcells in TSCs. (e) Efficiency distribution of 30 individual tandem devices.

and optimal vertical phase separation in the active layer. As a result, the binary OSC device with the TCB-treated SAM exhibited a superior PCE of 20.06% with an impressive FF of 80.64%. Moreover, we achieved a remarkable PCE of 26.09% in perovskite-organic TSCs using the TCB-treated SAM. This study provides a facile approach to regulate the ordered stacking of the SAM layer with solid additives to improve the performance of the photovoltaic device in both single junctions and tandem cells.

Author contributions

X. S., F. W. and G. Y. contributed equally to this work. X. S. wrote the original manuscript draft and made the in-depth data analysis. F. W. and G. Y. revised the original manuscript draft. X. D., J. L., Y. S., T. W. and X. X. tested the OSC devices and performed the EQE measurements. C. G., G. Z., W. L., X. O., M. Y. and L. Y. provided experimental support included *in situ* absorption, TPC, TPV and FLAS, *etc.* H. L., S. S., A. N. and H. Z. revised the manuscript. H. H. supervised experiments, provided resources, administration and funding. All authors read, corrected and approved the manuscript.

Data availability

The data supporting this article have been included as part of the ESI.†

Conflicts of interest

The authors declare no conflict of interest.

References

1 J. Wang, Y. Xie, K. Chen, H. Wu, J. M. Hodgkiss and X. Zhan, *Nat. Rev. Phys.*, 2024, **6**, 365.
2 L. Zhu, M. Zhang, Z. Zhou, W. Zhong, T. Hao, S. Xu, R. Zeng, J. Zhuang, X. Xue, H. Jing, Y. Zhang and F. Liu, *Nat. Rev. Electr. Eng.*, 2024, **1**, 581.
3 Y. Jiang, S. Sun, R. Xu, F. Liu, X. Miao, G. Ran, K. Liu, Y. Yi, W. Zhang and X. Zhu, *Nat. Energy*, 2024, **9**, 975.
4 L. Zhu, M. Zhang, G. Zhou, Z. Wang, W. Zhong, J. Zhuang, Z. Zhou, X. Gao, L. Kan, B. Hao, F. Han, R. Zeng, X. Xue, S. Xu, H. Jing, B. Xiao, H. Zhu, Y. Zhang and F. Liu, *Joule*, 2024, **8**, 3153.
5 C. Chen, L. Wang, W. Xia, K. Qiu, C. Guo, Z. Gan, J. Zhou, Y. Sun, D. Liu, W. Li and T. Wang, *Nat. Commun.*, 2024, **15**, 6865.
6 S. T. Guan, Y. K. Li, C. Xu, N. Yin, C. R. Xu, C. X. Wang, M. T. Wang, Y. X. Xu, Q. Chen, D. W. Wang, L. J. Zuo and H. Z. Chen, *Adv. Mater.*, 2024, **36**, e2400342.

7 Z. Chen, J. Ge, W. Song, X. Tong, H. Liu, X. Yu, J. Li, J. Shi, L. Xie, C. Han, Q. Liu and Z. Ge, *Adv. Mater.*, 2024, **36**, 2406690.

8 B. Fan, H. Gao, Y. Li, Y. Wang, C. Zhao, F. R. Lin and A. K. Y. Jen, *Joule*, 2024, **8**, 1443.

9 Y. Lin, Y. Firdaus, F. H. Isikgor, M. I. Nugraha, E. Yengel, G. T. Harrison, R. Hallani, A. El-Labban, H. Faber, C. Ma, X. Zheng, A. Subbiah, C. T. Howells, O. M. Bakr, I. McCulloch, S. D. Wolf, L. Tsetseris and T. D. Anthopoulos, *ACS Energy Lett.*, 2020, **5**, 2935.

10 C. Li, Y. Chen, Z. Zhang, C. Liu, F. Guo, W. Ahmad and P. Gao, *Energy Environ. Sci.*, 2024, **17**, 6157.

11 M. Li, M. Liu, F. Qi, F. R. Lin and A. K. Y. Jen, *Chem. Rev.*, 2024, **124**, 2138.

12 W. Jiang, D. Wang, W. Shang, Y. Li, J. Zeng, P. Zhu, B. Zhang, L. Mei, X.-K. Chen, Z.-X. Xu, F. R. Lin, B. Xu and A. K. Y. Jen, *Angew. Chem., Int. Ed.*, 2024, **63**, e202411730.

13 L. Zhang, Y. Wang, J. Wen, Y. Huang, J. Gao, Y. Duan, S. Park, W. Shin, Z. Ma, M. Liu, S. W. Cho, Y. Park, Y. M. Jung, H. Lee, W. Liu and Y. Liu, *Angew. Chem., Int. Ed.*, 2024, **63**, e202408960.

14 R. He, W. Wang, Z. Yi, F. Lang, C. Chen, J. Luo, J. Zhu, J. Thiesbrummel, S. Shah, K. Wei, Y. Luo, C. Wang, H. Lai, H. Huang, J. Zhou, B. Zou, X. Yin, S. Ren, X. Hao, L. Wu, J. Zhang, J. Zhang, M. Stolterfoht, F. Fu, W. Tang and D. Zhao, *Nature*, 2023, **618**, 80.

15 X. Sun, X. Ding, F. Wang, J. Lv, C. Gao, G. Zhang, X. Ouyang, G. Li and H. Hu, *ACS Energy Lett.*, 2024, **9**, 4209.

16 W. Guo, J. Li, H. Cen, J. Duan, Y. Yang, X. Yang, H. Dong, Z. Wu and J. Xi, *Adv. Energy Mater.*, 2024, **14**, 2401303.

17 J. Wang, Y. Wang, P. Bi, Z. Chen, J. Qiao, J. Li, W. Wang, Z. Zheng, S. Zhang, X. Hao and J. Hou, *Adv. Mater.*, 2023, **35**, 2301583.

18 T. Chen, Y. Zhong, T. Duan, X. Tang, W. Zhao, J. Wang, G. Lu, G. Long, J. Zhang, K. Han, X. Wan, B. Kan and Y. Chen, *Angew. Chem., Int. Ed.*, 2024, e202412983, DOI: **10.1002/anie.202412983**.

19 L. Tu, H. Wang, W. Duan, R. Ma, T. Jia, T. A. Dela Peña, Y. Luo, J. Wu, M. Li, X. Xia, S. Wu, K. Chen, Y. Wu, Y. Huang, K. Yang, G. Li and Y. Shi, *Energy Environ. Sci.*, 2024, **17**, 3365.

20 X. J. Cao, J. X. Guo, Z. X. Li, X. Q. Bi, H. Z. Liang, Z. Xiao, Y. X. Guo, X. Y. Jia, Z. Xu, K. Q. Ma, Z. Y. Yao, B. Kan, X. J. Wan, C. X. Li and Y. S. Chen, *ACS Energy Lett.*, 2023, **8**, 3494.

21 M. Y. Jiang, H. F. Zhi, B. Zhang, C. C. Yang, A. Mahmood, M. Zhang, H. Y. Woo, F. J. Zhang, J. L. Wang and Q. S. An, *ACS Energy Lett.*, 2023, **8**, 1058.

22 J. Fu, P. W. K. Fong, H. Liu, C.-S. Huang, X. Lu, S. Lu, M. Abdelsamie, T. Kodalle, C. M. Sutter-Fella, Y. Yang and G. Li, *Nat. Commun.*, 2023, **14**, 1760.

23 T. Lu and S. Manzetti, *Struct. Chem.*, 2014, **25**, 1521.

24 T. Lu and F. Chen, *J. Comput. Chem.*, 2012, **33**, 580.

25 S. Yang, Z. Chen, J. Zhu, D. Yang, H. Wang, P. Ding, J. Wu, P. Yan, L. Xie, F. Chen, Y. Wang, J. Zhang and Z. Ge, *Adv. Mater.*, 2024, **36**, 2401789.

26 T. Lu and Q. Chen, in *Comprehensive Computational Chemistry*, ed. M. Yáñez and R. J. Boyd, Elsevier, Oxford, 1st edn, 2024, p. 240, DOI: **10.1016/B978-0-12-821978-2.00076-3**.

27 X. Song, K. Zhang, R. J. Guo, K. Sun, Z. X. Zhou, S. L. Huang, L. Huber, M. Reus, J. G. Zhou, M. Schwartzkopf, S. Roth, W. Z. Liu, Y. Liu, W. G. Zhu and P. Müller-Buschbaum, *Adv. Mater.*, 2022, **34**, e2200907.

28 C.-C. Peng, S.-Y. Yang, H.-C. Li, G.-H. Xie, L.-S. Cui, S.-N. Zou, C. Poriel, Z.-Q. Jiang and L.-S. Liao, *Adv. Mater.*, 2020, **32**, 2003885.

29 A. Al-Ashouri, A. Magomedov, M. Roß, M. Jošt, M. Talaikis, G. Chistiakova, T. Bertram, J. A. Márquez, E. Köhnen, E. Kasparavičius, S. Levcenco, L. Gil-Escrig, C. J. Hages, R. Schlatmann, B. Rech, T. Malinauskas, T. Unold, C. A. Kaufmann, L. Korte, G. Niaura, V. Getautis and S. Albrecht, *Energy Environ. Sci.*, 2019, **12**, 3356.

30 N. Zhao, C. M. Yang, F. G. Bian, D. Y. Guo and X. P. Ouyang, *J. Appl. Crystallogr.*, 2022, **55**, 195.

31 A. Gibaud, S. Dourdain, O. Gang and B. M. Ocko, *Phys. Rev. B: Condens. Matter Mater. Phys.*, 2004, **70**, 161403.

32 D. Liu, Z. He, Y. Su, Y. Diao, S. C. B. Mannsfeld, Z. Bao, J. Xu and Q. Miao, *Adv. Mater.*, 2014, **26**, 7190.

33 W. Li, T. Zhou, Z. Zhang, L. Li, W. Lian, Y. Wang, J. Lu, J. Yan, H. Wang, L. Wei and Q. Cheng, *Science*, 2024, **385**, 62.

34 Y. F. Qi, M. Almtiri, H. Giri, S. Jha, G. R. Ma, A. K. Shaik, Q. Q. Zhang, N. Pradhan, X. D. Gu, N. I. Hammer, D. Patton, C. Scott and Q. L. Dai, *Adv. Energy Mater.*, 2022, **12**, 2202713.

35 Z. Chen, S. Zhang, T. Zhang, J. Dai, Y. Yu, H. Li, X. Hao and J. Hou, *Joule*, 2024, **8**, 1723.

36 K. Zhao, Q. Liu, L. Yao, C. Değer, J. Shen, X. Zhang, P. Shi, Y. Tian, Y. Luo, J. Xu, J. Zhou, D. Jin, S. Wang, W. Fan, S. Zhang, S. Chu, X. Wang, L. Tian, R. Liu, L. Zhang, I. Yavuz, H.-f Wang, D. Yang, R. Wang and J. Xue, *Nature*, 2024, **632**, 301.

37 Q. Zhao, B. Zhang, W. Hui, Z. Su, H. Wang, Q. Zhang, K. Gao, X. Zhang, B.-h Li, X. Gao, X. Wang, S. De Wolf, K. Wang and S. Pang, *J. Am. Chem. Soc.*, 2024, **146**, 19108.

38 H. Xu, A. Sharma, J. Han, B. P. Kirk, A. R. Alghamdi, F. Xu, Y. Zhang, A.-H. Emwas, G. Hizalan, S. De Wolf, M. R. Andersson, G. G. Andersson and D. Baran, *Adv. Energy Mater.*, 2024, **14**, 2401262.

39 X. Yu, P. Ding, D. Yang, P. Yan, H. Wang, S. Yang, J. Wu, Z. Wang, H. Sun, Z. Chen, L. Xie and Z. Ge, *Angew. Chem., Int. Ed.*, 2024, **63**, e202401518.

40 R. Zeng, L. Zhu, M. Zhang, W. K. Zhong, G. Q. Zhou, J. X. Zhuang, T. Y. Hao, Z. C. Zhou, L. B. Zhou, N. Hartmann, X. A. Xue, H. Jing, F. Han, Y. M. Bai, H. B. Wu, Z. Tang, Y. C. Zou, H. M. Zhu, C. C. Chen, Y. M. Zhang and F. Liu, *Nat. Commun.*, 2023, **14**, 4148.

41 X. Sun, C. Zhang, Y. Yao, J. Lv, J. Yao, X. Ding, M. Lu, L. Zhu, G. Zhang, H. Lin, Y. Shi, K. Wang, C. Yang, X. Ouyang, H. Hu, I. McCulloch and Y. Lin, *Adv. Funct. Mater.*, 2024, **34**, 2406060.

42 B. Hu, S. Gao, X. Wang, F. Cao, Y. Chen, J. Zhang, L. Bu, X. Song and G. Lu, *Energy Environ. Sci.*, 2024, **17**, 7803.

43 L. Chen, J. Yi, R. Ma, L. Ding, T. A. Dela Pena, H. Liu, J. Chen, C. Zhang, C. Zhao, W. Lu, Q. Wei, B. Zhao, H. Hu, J. Wu, Z. Ma, X. Lu, M. Li, G. Zhang, G. Li and H. Yan, *Adv. Mater.*, 2023, **35**, e2301231.

44 X. Sun, J. Lv, X. Ding, C. Gao, G. Zhang, J. Zeng, C. Zou, W. Liu, S. Zhao, X. Ouyang, C. Yang, H. Hu and H. Chen, *ACS Mater. Lett.*, 2024, **6**, 3282.

45 C. Zhao, Y. Wang, K. Sun, C. Gao, C. Li, Z. Liang, L. Zhu, X. Sun, D. Wu, T. Yang, Z. Tang, P. You, C. Xie, Q. Bai, C. Li, J. Yi, H. Hu, S. Li, H. Yan and G. Zhang, *Mater. Sci. Eng., R*, 2024, **160**, 100828.

46 Z. Chen, S. Zhang, J. Ren, T. Zhang, J. Dai, J. Wang, L. Ma, J. Qiao, X. Hao and J. Hou, *Adv. Mater.*, 2024, **36**, 2310390.

47 X. Jiang, S. Qin, L. Meng, G. He, J. Zhang, Y. Wang, Y. Zhu, T. Zou, Y. Gong, Z. Chen, G. Sun, M. Liu, X. Li, F. Lang and Y. Li, *Nature*, 2024, **635**, 860.

48 X. Cui, G. Xie, Y. Liu, X. Xie, H. Zhang, H. Li, P. Cheng, G. Lu, L. Qiu and Z. Bo, *Adv. Mater.*, 2024, **36**, e2408646.

49 X. Wu, D. Zhang, B. Liu, Y. Wang, X. Wang, Q. Liu, D. Gao, N. Wang, B. Li, L. Wang, Z. Yu, X. Li, S. Xiao, N. Li, M. Stolterfoht, Y.-H. Lin, S. Yang, X. C. Zeng and Z. Zhu, *Adv. Mater.*, 2024, **36**, e2410692.

50 S. Wu, Y. Yan, J. Yin, K. Jiang, F. Li, Z. Zeng, S.-W. Tsang and A. K. Y. Jen, *Nat. Energy*, 2024, **9**, 411.

51 Z. Zhang, W. Chen, X. Jiang, J. Cao, H. Yang, H. Chen, F. Yang, Y. Shen, H. Yang, Q. Cheng, X. Chen, X. Tang, S. Kang, X.-m Ou, C. J. Brabec, Y. Li and Y. Li, *Nat. Energy*, 2024, **9**, 592.

52 X. Guo, Z. Jia, S. Liu, R. Guo, F. Jiang, Y. Shi, Z. Dong, R. Luo, Y.-D. Wang, Z. Shi, J. Li, J. Chen, L. K. Lee, P. Müller-Buschbaum, D. S. Ginger, D. J. Paterson and Y. Hou, *Joule*, 2024, **8**, 2554.

This journal is © The Royal Society of Chemistry 2025

Energy Environ. Sci., 2025, **18**, 2536–2545 | **2545**